Target selection and imaging requirements for JWST fine phasing

Joseph J. Green[a*], Bruce H. Dean[b], Catherine M. Ohara[a] and Yan Zhang[a]

[a]Jet Propulsion Laboratory, California Institute of Technology
[b]Goddard Space Flight Center, National Aeronautics and Space Administration

ABSTRACT

To achieve and maintain the fine alignment of its segmented primary mirror the James Webb Space Telescope (JWST) plans to use focus-diverse wavefront sensing (WFS) techniques with science camera imagery. The optical requirements for JWST are such that the error contribution from the WFS itself must be limited 10nm rms over all the controllable degrees of freedom of the telescope. In this paper, we will explore the requirements on the target selection and imaging requirements necessary to achieve the desired level of WFS accuracy. Using Monte Carlo simulations we explore the WFS error as a function of wavefront aberrations level, defocus-diversity level, optical bandwidth and imaging signal-to-noise ratio to establish the key imaging requirements. By taking into account practical integration time limits along with the distribution of the defocused point-spread functions, we establish the bright and faint star magnitude limits suitable for WFS target selection.

Keywords: wavefront sensing, focus diversity, James Webb Space Telescope

1. INTRODUCTION

NASA is planning to launch the James Webb Space Telescope (JWST), an infrared large-aperture telescope, at the beginning of the next decade. The JWST design is a segmented, 6.5 meter, off-axis, three-mirror anastigmat telescope with a primary mirror composed of 18 hexagonal segments. With its well-aligned mirrors, large primary mirror collecting area and infrared detectors, JWST will enable the direct observation of the first stars and galaxies in the universe. General information about the JWST science and technology programs can be found at http://jwst.gsfc.nasa.gov.

During its commissioning, JWST will using image-based wavefront sensing (WFS) and control methodologies to align and figure the primary mirror segments as well as to align the secondary mirror[1]. The last stage of WFS and control is ultimately responsible establishing final fine alignment of the telescope optics that limits the final image quality. As such, the desired accuracy of this WFS process is 10nm rms over all the controllable degrees of freedom on JWST. The baseline WFS methodology for JWST fine phasing is called the Modified Gerchberg-Saxton (MGS) WFS algorithm[2]. This image-based algorithm processes a pupil image along with a diverse set of defocused point-spread function (PSF) measurements into an estimate of the exit-pupil phase aberrations. Using the JWST Phase Retrieval Camera[2] along with MGS WFS algorithm, Green et al has experimentally demonstrated the capacity to sense the wavefront to the $\lambda/200$ accuracy level[4]. For the Terrestrial Planet Finder (TPF) program, they developed methods of overcoming many of the limiting systematic factors to MGS algorithm[5] and on the TPF High Contrast imaging Testbed[6] have demonstrated $\lambda/10{,}000$ wavefront repeatability[7].

While this demonstrated level of performance far exceeds the JWST requirements, we have found that the WFS accuracy remains tied to many systematic factors including the level focus diversity, the magnitude of the wavefront error (WFE) being sensed and the presence of an optical bandwidth. In this paper we explore the impacts of

* Further author information: (Send correspondence to J.J.G.)
J.J.G.: E-mail: Joseph.J.Green@jpl.nasa.gov, 4800 Oak Grove Dr., M/S 306-336, Pasadena CA 91109,
B.H.D.: E-mail: Bruce.H.Dean@gsfc.nasa.gov, M/S 551.0, Greenbelt MD 20771,
C.M.O.: E-mail: Catherine.M.Ohara@jpl.nasa.gov, 4800 Oak Grove Dr., M/S 301-486, Pasadena CA 91109,
Y.Z.: E-mail: Yan.Zhang@jpl.nasa.gov, 4800 Oak Grove Dr., M/S 301-486, Pasadena CA 91109,

systematic effects and noise upon the JWST WFS accuracy. In the next section, we describe details of the imaging model we employed in our simulations and summarize the systematic incorporated errors sources. In Section 3, we present results from our Monte Carlos study into the impacts from systematic effects including optical bandwidth, line-of-sight jitter, finite pixel size and uncalibrated F/# variations (from using lenses for focus diversity). In Section 4, we present the stochastic impacts from read-noise, photon noise and detection calibrations error. From these studies we establish bounds on the desire defocus levels, optical bandwidth and integrated flux. In Section 5 we apply these bounds to ascertain the bright and faint limit on WFS star magnitudes. By looking at the extent of the defocused PSFs we also establish constraints on nearby objects within the WFS target field.

2. JWST OPTICAL SYSTEM MODEL

For this study, we employed an exit-pupil model[8] to represent JWST segmented architecture. Because the segments gaps are small relative to the segment sizes, we constructed an exit-pupil amplitude function using the gray pixel approximation method[9]. Using the exact far-field description of a single segment, we computed the net far-field pattern caused by the 18 segments over the field of view by aggregating individual patterns; each induced with the appropriate amount of phase tilt. Taking the Fourier transform of the result yields the full, segmented pupil function with appropriate apodization to represent the gaps. To account for the secondary mirror supports, we simply applied an appropriate binary mask to force the pupil amplitude to be zero in the shadow of the support. The high-resolution pupil function we developed for this study along with an example of a realization of the optical errors is shown in Figure 1. The WFE shown in this figure includes aberrations representative of segment and secondary mirror misalignments as well as segment figure and mirror fabrication errors.

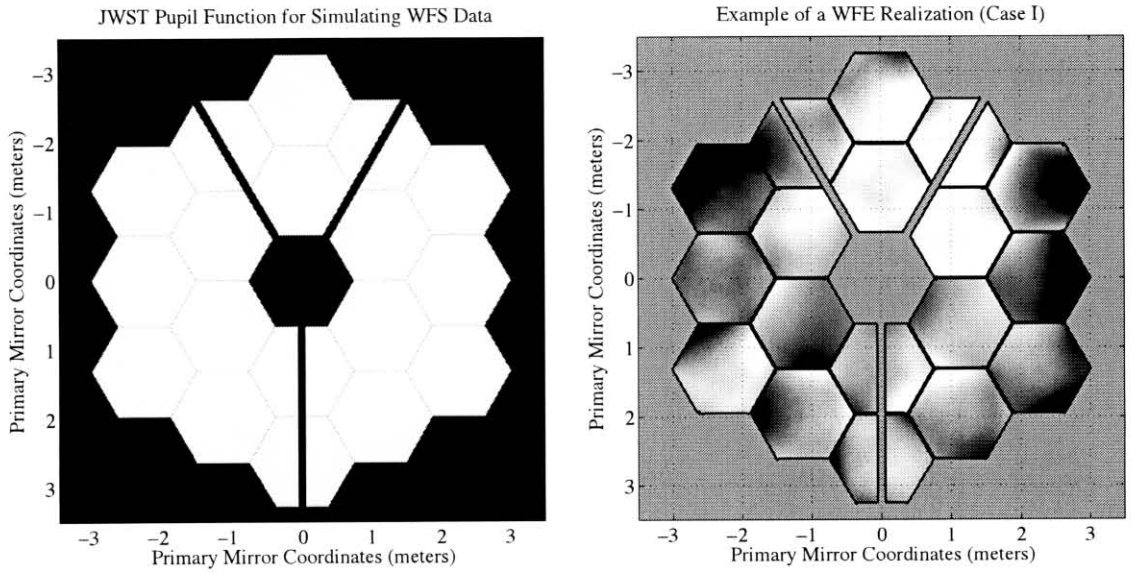

Figure 1: The gray pixel representation of the JWST pupil is shown (left) along with an example of an aberrations realization (right) that includes errors from segment and secondary mirror misalignmets as well as mirror fabrication errors. The wavefront error realization is shown with a ±200nm linear intensity scaling and has 130nm rms.

In our Monte Carlo study we consider four different aberrations scenarios representing different states of JWST. The first state contains alignment and figure errors that are consistent with meeting the high level JWST imaging requirements. The optical path difference (OPD) map shown in Figure 1 is an example of a realization from this case. The other cases represent JWST states with increased aberration mixtures before the final alignment is established. Descriptions of these states along with the ensemble statistics from the 20 realizations are shown in Table 1.

Table 1: Statistics of the aberration cases are shown below along with descriptions of the respective JWST states. The statistics represent the ensemble mean and standard deviation computed over the 20 realizations used for the study.

Aberration Case	RMS Aberration Statistics (nm WF)	Description of Aberration Case
I	118.8 ± 21.2	Aberrations constistent with JWST Image Quality Requirements
II	155.1 ± 27.8	50% higher global low-order aberations
III	143.6 ± 19.6	50% higher segment alignment and figure errors
IV	170.6 ± 25.0	50% higher low-order and segment aberations

In Figure 2 we show simulated defocused PSF measurements that are the result of the OPD shown in Figure 1. The PSF calculations are not monochromatic but rather 1% narrowband measurements are composed of 11 monochromatic calculations about a central wavelength of 2.12μm. The distribution of light in the defocus PSFs are the result of the optical errors shown in Figure 1 and the defocus aberration induced by theoretical lenses. Aside from the aberrations and the effects from the optical bandwidth, the PSFs in Figure 1 are impacted by a variety of simulated systematic errors. Refer to Table 2 in the next section for a complete list of these errors sources assumed in our investigation.

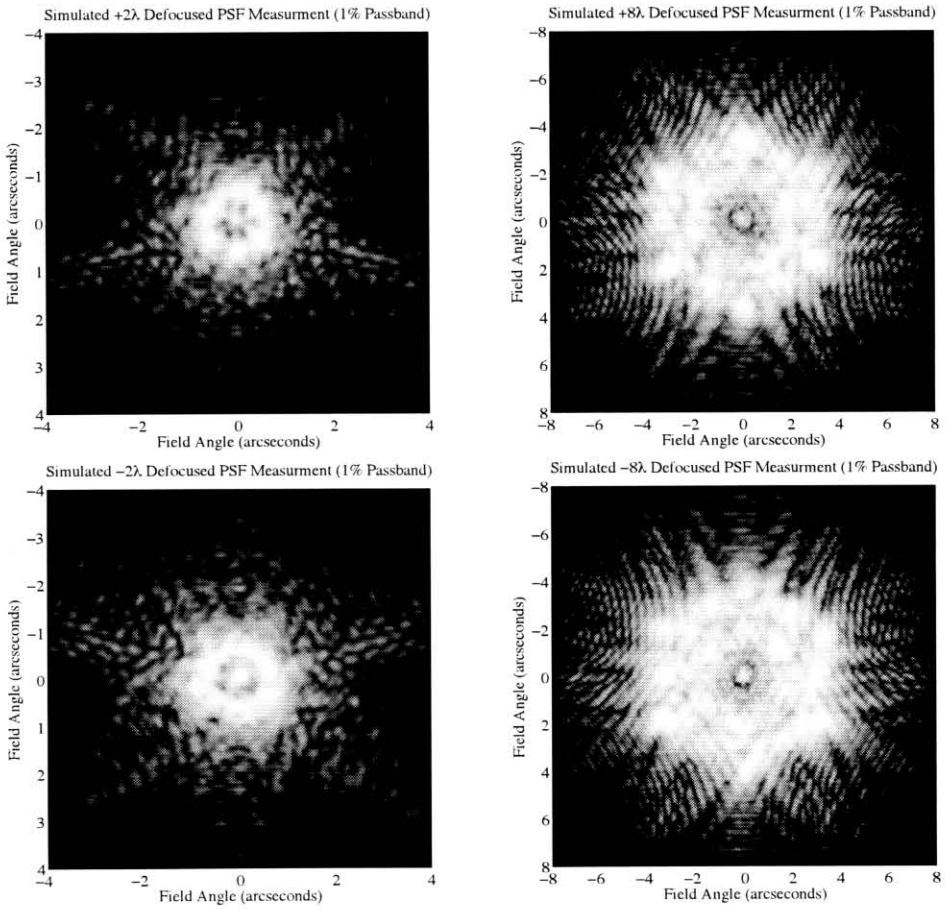

Figure 2: Example of simulated defocused PSF measurements are shown. They are narrowband ($\Delta\lambda/\lambda$=1%) 2.12μm PSFs with ±2 waves (peak-to-valley) of defocus (left column) and ±8 waves of defocus (right-column). To better illustrate the PSF structure, the intensity shown is logarithmically stretched over tope 3 orders of magnitude. Additionally, the ±2 wave PSFs are shown in a 8″ × 8″ field of view while the ±8 PSF are shown in a 16″ × 16″ field of view.

3. WFS PERFORMANCE IN THE PRESENCE OF SYSTEMATIC ERRORS

Using a pair of simulated defocused PSF measurements and knowledge about the pupil support, we can compute an estimate of the OPD using the MGS algorithm. Typically, the pupil support knowledge comes from a pupil image. In our study, we use a down-sampled binary version of the pupil function that does not have a representation for segment gaps. From the standpoint of the algorithm this is a model-mismatch error and will result in a level of WFS error. In our earlier work, we have shown the effect can be made minimal by using symmetric defocus levels in the PSF measurements[5]. Other model mismatch errors to the MGS algorithm include optical bandwidth, line-of-sight jitter, finite detector pixel size and lens-induced F/# variations. The impacts from these effects are also mitigated by various degrees through the use of symmetrically defocused PSF measurements. Table 2 summarizes all the systematic errors sources and the level (or range) at which they are included in the simulations.

Table 2: List of systematic error sources used in our study

Description of Error	Value	Units
Optical Bandwith	1-10	$\Delta\lambda/\lambda$ x 100
Line of Sight Jitter	5.00	mas/axis (1-σ)
Finite Pixel Size	18	μm/pixel
Lens-Induced F/# Variation	0.01-0.04	% of nominal design
Quantization Error	16	bits/pixel
Conversion Gain	1.5	electrons/DN

In Figure 3, we present estimates of the JWST OPD from the ±2 wave and ±8 wave defocused PSF pairs that are shown in Figure 2. Clearly, there are differences in the quality of the estimates. Most notably, the resolution of the ±8 wave OPD appears to be much higher. To gauge their absolute accuracy, we resample the actual OPD used to generate the simulated PSF data onto the same grid as the estimates. From this, we compute the WFS error in two ways. The raw differences between the resampled truth and an estimate yield the error over the entire estimate resolution. For JWST, however, we are concerned with the WFS error that affects the subsequent wavefront control. Thus we filter the difference between the truth and an estimate by fitting out the first 21 low-order Zernike modes[10] (includes out to the 5th order radial terms) along with the first 6 modes per segment. The result is the controllable WFS error that we wish to minimize through our choice of imaging parameters. Figure 4, shows the WFS error over the entire estimate resolution as well over only the controllable degrees of freedom.

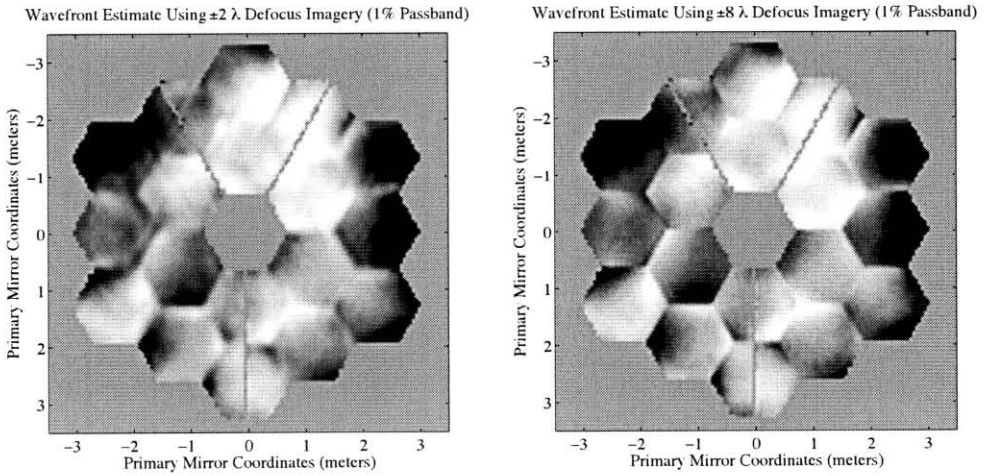

Figure 3: Estimates of the JWST OPD from the ±2 wave defocus PSF pair (left) and the ±8 wave pair (right). As in Figure 1, the OPDs are shown with a linear intensity scale stretched over ±200nm.

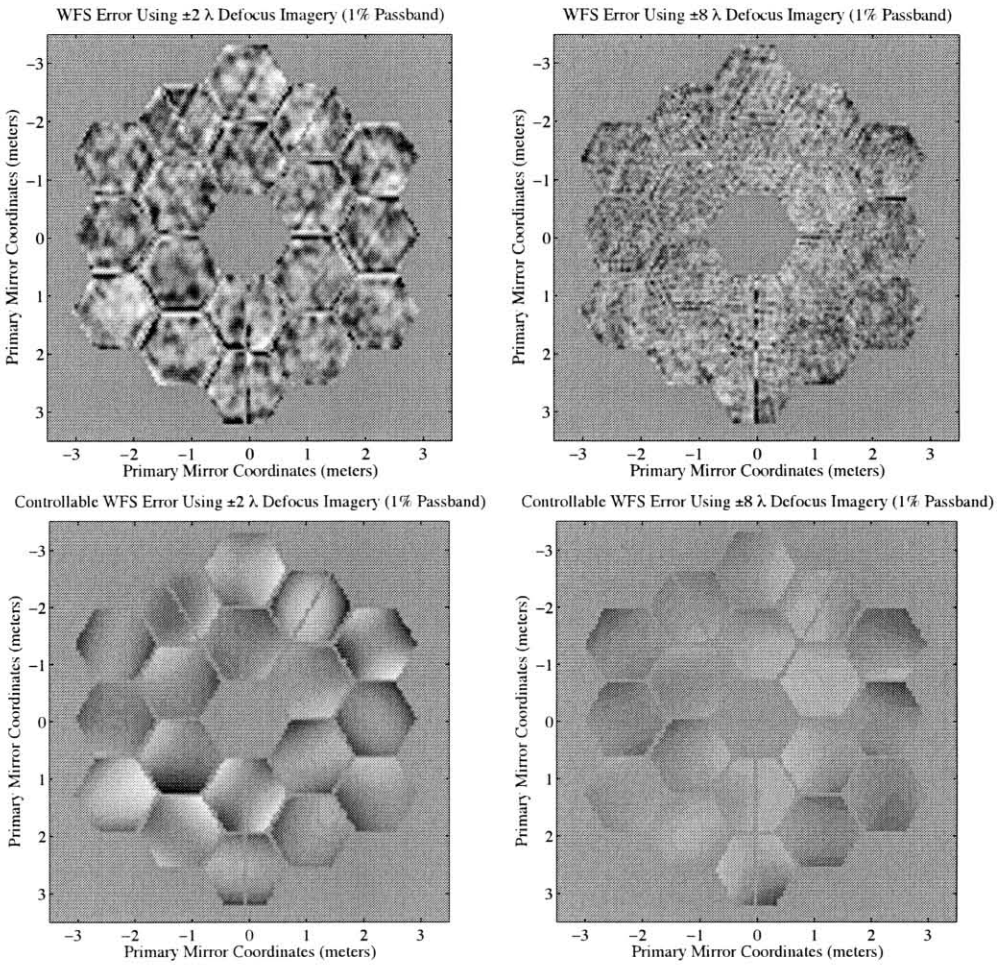

Figure 4: WFS error resulting from using the ±2 wave (left-column) and ±8 wave (right-column) defocus PSF pairs. The WFS error in these images has been linearly stretched over a range of ±50nm. The top row shows the error over all spatial frequencies. The total WFS error is 15.6nm rms for the ±2 wave and 9.9nm rms for the ±8 wave estimate. The bottom row shows the controllable WFS error, which is 8.2nm rms for the ±2 wave and 4.1nm rms for the ±8 wave estimate

The errors shown are the result of processing the PSF that are corrupted by all the systematic error sources but none of the stochastic error sources. There is neither read-noise nor Poisson noise introduced into the PSFs and thus the resulting WFS error represents the expected performance in the limit of infinite integration times and perfect calibration. In the next section we will explore the impacts that these and other noise sources have upon the WFS accuracy.

Figure 4 is a sample realization out of our Monte Carlo studies. The scatter plots in Figure 5 show the controllable WFS error over the ensemble of realizations for the two extremes of the optical bandwidth studied. Each point on a plot is the resulting estimation error from using a pair of PSFs created by the particular aberration instance and choice of a defocus levels. As in the single example shown earlier, the only WFS error sources admitted are those that are resulting from systematic effects. By comparing the two plots, it is clear that a larger optical bandwidth reduces the accuracy of the WFS. Furthermore, the estimation error resulting from using less defocused PSFs are generally higher, particularly when imaging with larger optical bandwidths.

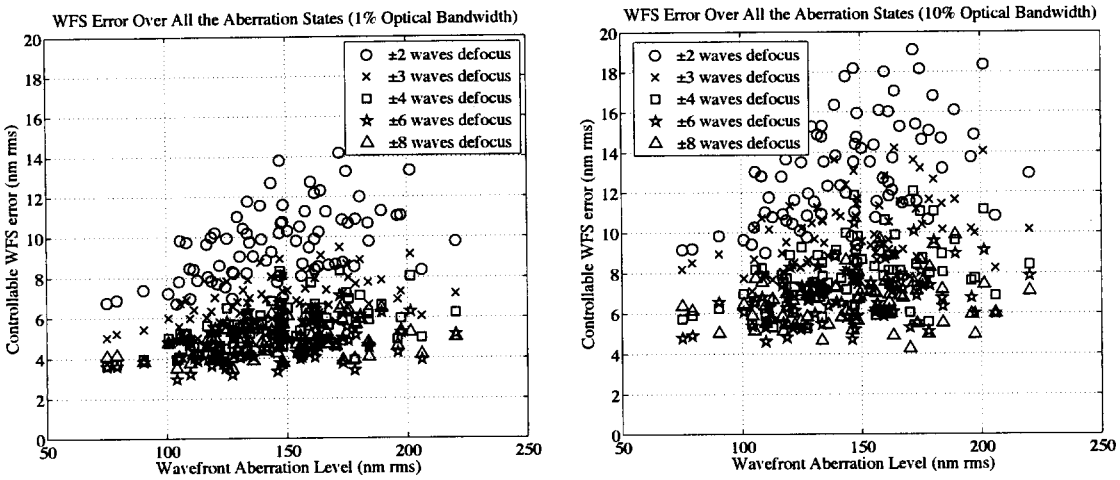

Figure 5: The controllable WFS error from all aberrations realizations and defocus levels studied are shown. Presented is the controllable WFS error resulting from the systematic errors including a 1% optical passband (left) and 10% optical passband (right).

Table 3 presents the ensemble statistics for all the cases studies. The average controllable WFS error ± one standard deviation is listed as a function of defocus and optical bandwidth for the four aberrations cases. The other systematic error sources listing in Table 2 were present at their indicated levels. Figure 6 plots the ensemble statistics, illustrating the impact of optical bandwidth more clearly. Here the WFS performance is plotted for two of the four aberrations cases. In each of the plots, the controllable WFS error is shown as a function of optical bandwidth for the 5 defocus level pairs. From these plots we can see that WFS accuracy is poorest when ±2 wave defocused PSFs are used. Here, the WFS performance is the most sensitive to optical bandwidth as well as the magnitude of the aberration being sensed. Estimates derived from the ±6 wave and ±8 wave imagery performed similarly, with the ±6 wave yielding the most accurate estimates at the lowest aberrations levels. It may well be the case that the ±6 wave imagery is the most

Table 3: Ensemble statistics from the systematic error study are shown. The average rms WFS error ± one standard deviation over all defocus levels and optical bandwidths for the 4 different aberration cases. Each entry in the table is computed from the 20 aberrations realizations.

Aberration Case	Optical Bandwidth	Aggregate Statistics of the Controllable WFSE (nm rms)				
		±2 λ	±3 λ	±4 λ	±6 λ	±8 λ
I	1%	8.0 ± 0.9	5.5 ± 0.5	4.5 ± 0.5	3.9 ± 0.5	4.3 ± 0.5
	2%	8.1 ± 0.9	5.6 ± 0.5	4.6 ± 0.5	4.0 ± 0.5	4.3 ± 0.5
	5%	8.7 ± 1.0	6.2 ± 0.5	4.9 ± 0.6	4.3 ± 0.6	4.5 ± 0.6
	10%	10.8 ± 1.3	8.2 ± 0.8	6.5 ± 0.8	5.8 ± 0.7	5.8 ± 0.7
II	1%	8.6 ± 1.0	6.0 ± 0.5	4.9 ± 0.6	4.2 ± 0.5	4.6 ± 0.6
	2%	8.7 ± 1.0	6.1 ± 0.5	4.9 ± 0.6	4.3 ± 0.6	4.6 ± 0.6
	5%	9.5 ± 1.3	6.8 ± 0.6	5.3 ± 0.7	4.7 ± 0.6	4.8 ± 0.7
	10%	11.7 ± 1.4	8.8 ± 0.9	7.0 ± 0.9	6.0 ± 0.8	6.0 ± 0.8
III	1%	10.8 ± 1.3	7.4 ± 0.8	6.1 ± 0.8	5.2 ± 0.7	5.4 ± 0.6
	2%	10.9 ± 1.3	7.5 ± 0.8	6.1 ± 0.9	5.2 ± 0.8	5.4 ± 0.6
	5%	11.8 ± 1.5	8.3 ± 0.9	6.6 ± 1.0	5.7 ± 0.8	5.7 ± 0.7
	10%	14.8 ± 1.9	10.9 ± 1.3	8.8 ± 1.2	7.6 ± 1.1	7.3 ± 1.0
IV	1%	11.3 ± 1.3	7.9 ± 0.9	6.4 ± 0.9	5.4 ± 0.8	5.6 ± 0.6
	2%	11.4 ± 1.3	8.0 ± 0.9	6.5 ± 0.9	5.5 ± 0.8	5.7 ± 0.6
	5%	12.2 ± 1.4	8.9 ± 1.0	7.0 ± 1.1	6.1 ± 0.9	6.0 ± 0.8
	10%	15.4 ± 1.9	11.5 ± 1.5	9.1 ± 1.3	7.9 ± 1.1	7.5 ± 1.1

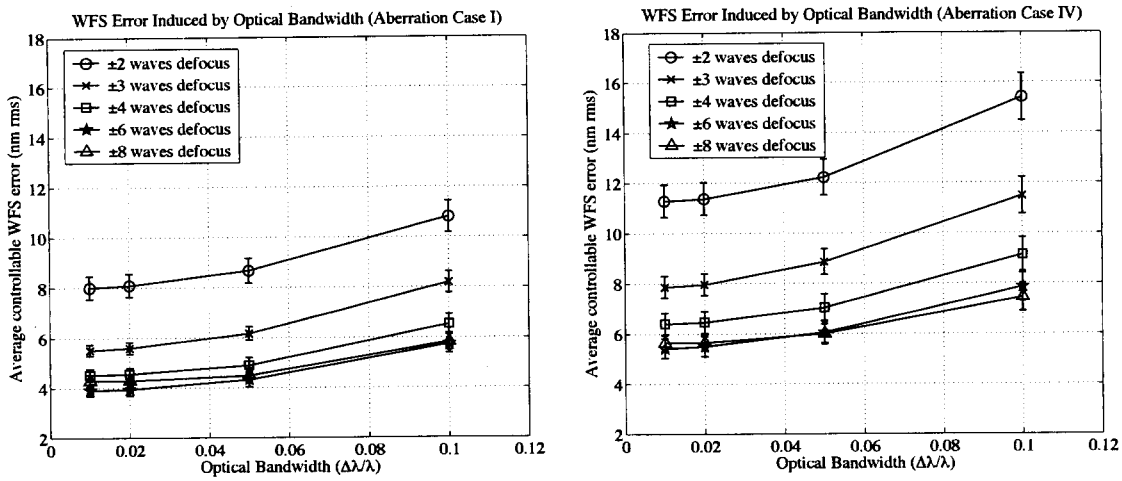

Figure 6: The ensemble statistics for the controllable WFS error as a function of optical bandwidth are plotted for two of the four aberrations cases considered in this study. The data points represent the ensemble mean for each optical bandwidth case and the bars have a length equaling one standard deviation about their respective mean. Aside from the optical bandwidth, all other systematic error sources are present during the simulation.

sensitive to the spatial frequencies tied to the JWST controllable degrees of freedom. At higher levels of defocus, the sensitivity at the lowest spatial frequencies diminished. This connection between the level defocus in the PSF measured and the spatial frequency sensitivity has been both theoretically derived[11] and experimentally demonstrated[7].

4. WFS PERFORMANCE IN THE PRESENCE OF STOCHASTIC ERRORS

In the previous section, we examined the impact of the expected systematic errors upon the WFS accuracy over the JWST controllable degrees of freedom. The results indicate that with the proper selection of defocus levels and optical bandwidth, the 10nm WFS accuracy requirement can be met. Nevertheless, these results we obtained in the absence of calibration error, detector noise and finite integrations time. Such stochastic effects will further diminish the fidelity of the OPD estimates that are measured in practice. In this section we will study their impacts.

In Table 4, we list the type of stochastic error sources and the magnitude or magnitudes that they are introduced into simulation PSF imagery. With the exception of the integration time, all the noise sources are held at a constant level. With respect to the integration time, we scaled the integration time to allow defocused PSFs to be formed from a collection of 10^5 to 10^8 photons per PSF. The read noise was introduced by adding signal-independent Gaussian noise and the dark current and Zodiacal light were introduced by adding Poisson noise at the appropriate level. Introducing an additional signal-dependent Gaussian noise source, we simulated the calibration gain error. By studying these noises source in the presence a fixed selection of systematic impacts, we can obtain a more complete understanding the imaging requirements necessary to achieve the JWST requirements.

Rather that go through all the aberrations cases in the previous study, we took a single aberration realization (the one shown in Figure 1) and along with a set of systematic errors (i.e. 1% optical passband) to be fixed parameters of this study. Using the noise sources just described, we create PSFs at various levels of defocus and integrated flux and collect statistics on the controllable WFS performance from the MGS estimates. Table 5 lists the resulting ensemble statistics collected over the 15 noise realizations obtained for each defocus level and integrated flux pair. The results reveal tradeoffs between defocus and total integrated flux that can be made to achieve a particular level of controllable WFS accuracy.

Table 4: List of stochastic error sources used in the study.

Description of Stochastic Error	Value(s)	Units
Finite Integration Time	10^5-10^8	photons/PSF
Zodiacal Light	2x10^-3	phot/s/cm^2/μm/asec
Read-Noise	9.00	electrons rms
Dark Current	0.01	electrons/s/pix
Detector Gain Calibration Error	0.50	%/pix

At low levels of integrated flux, the WFS performance is superior at lower levels of defocus. Although the ±2 wave-defocused PSFs are the most spatially concentrated at the detector, yielding a high signal-to-noise ratio (SNR), the impact of the fixed systematic errors overwhelms the SNR benefit. Once again, we see that the ±6 wave-defocused PSF offers the best sensing of the JWST controllable WFE at high levels of integrate flux. To meet the WFS requirements with the minimum integrated flux, the ±4 wave-defocus performance may seem attractive. It achieves this, however, at point along its performance curve where its accuracy is quickly degrading with diminishing photon counts. This is not the most desirable operation point for stable WFS. The higher levels of defocus can yield better and *more stable* performance with a modest increase in integration time.

Table 5: Ensemble statistics from the stochastic error study are shown. The average rms WFE ± one standard deviations are listed over all defocus and integrated flux levels.

Log Integrated Flux	Aggregate Statistics of the Controllable WFSE (nm rms)				
	±2 λ	±3 λ	±4 λ	±6 λ	±8 λ
5.0	63.2 ± 5.9	73.9 ± 6.3	80.7 ± 2.8	102.0 ± 8.3	116.8 ± 9.3
5.5	32.7 ± 3.7	39.5 ± 3.3	48.1 ± 4.5	63.3 ± 5.7	79.6 ± 6.5
6.0	14.7 ± 0.8	15.2 ± 0.9	17.8 ± 2.1	25.0 ± 2.6	28.6 ± 3.4
6.5	9.4 ± 0.3	8.0 ± 0.4	7.4 ± 0.5	8.6 ± 0.8	11.0 ± 2.4
7.0	8.3 ± 0.2	6.0 ± 0.2	5.5 ± 0.3	5.3 ± 0.5	6.1 ± 0.6
7.5	8.3 ± 0.1	5.5 ± 0.1	4.8 ± 0.1	4.4 ± 0.2	5.0 ± 0.2
8.0	8.2 ± 0.0	5.4 ± 0.0	4.8 ± 0.1	4.1 ± 0.1	4.8 ± 0.1

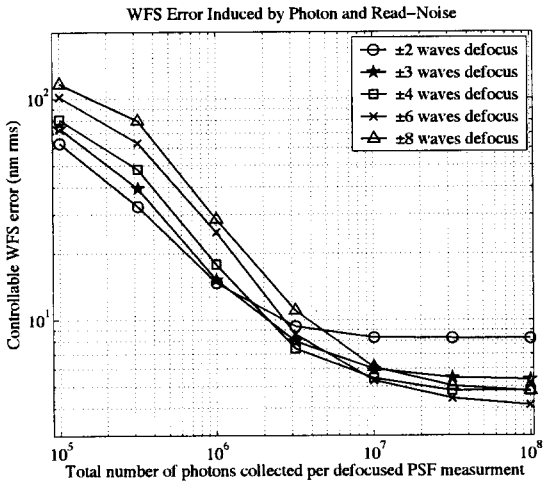

Figure 7: The ensemble statistics for the controllable WFS error as a function of integrated flux are plotted over all the defocus levels studied. At integrated flux levels less than 10^7 the stochastic errors dominate the WFS performance. Above this level, the principle contributors to the controllable WFS error are the systematic errors sources.

5. TARGET SELECTION FOR JWST WFS

With a notion of the appropriate levels of defocus, optical bandwidth and integrated flux, we can set some practical limits on suitable star brightness. There are really two bounds to consider. The bright limit is set by the combination of shortest allowable integration time, the detector well depth and the distribution of the light being measured. The faint limit is set by the total number of photons we wish to collect and the longest integration time that we are willing to endure. In our calculations we assumed the 25 m^2 primary mirror collecting area, a net 50% telescope and detector efficiency, and stars with A0V flux densities[12]. Supposing that we are imaging at a central wavelength of 2.12μm we compute the net flux density and integrate it over the desired optical passband. With a presumed minimum integration time of 0.5 seconds (set by full-well and the detector read-out rate) and a maximum integration time of 1000 seconds (set by our patience and desire to minimize cosmic ray hits) we can establish acceptable ranges for star brightness.

In Table 6 we show bright and faint magnitude limit for candidate WFS stars. The bright limit corresponds to the highest magnitudes allowable without saturating the detector within 0.5 seconds. For this we assumed we set a maximum threshold of 75,000 electrons per pixel. Depending upon defocus level and optical bandwidth, the bright limit varies. The values shown in the table represent the average bright limit computed over the ensemble of PSF realizations. The faint limit was computed by the goal of collecting 10^8 photons per defocused PSF measurement within 1000 seconds. At this level of integrated flux, the contribution from the noise sources is minimal. By reducing the desired photon count to 10^7 we could increase the faint-limit by 2.5 magnitudes with a mild increase in the WFS error performance and slight reduction in the WFS error stability.

Table 6: Bright and faint stellar magnitude constraints on JWST WFS targets. The bright limit is based on collecting no more than 75,000 net photons per pixel within 0.5 seconds. The faint limit is based on collecting 10^8 photons per PSF within 1000 seconds.

Optical	Bright Limit (Tmin = 0.5 sec)					Faint Limit
Bandwidth	±2 λ	±3 λ	±4 λ	±6 λ	±8 λ	(Tmax = 1000 sec)
1%	3.94	3.09	2.50	1.66	1.10	10.43
2%	4.71	3.91	3.31	2.47	1.84	11.17
5%	5.70	4.90	4.30	3.49	2.97	12.16
10%	6.49	5.76	5.13	4.28	3.72	12.91

As a final consideration for WFS target selection, we to consider the level of target isolation needed for any candidate star. Looking back at Figure 2, we can get sense of the defocused PSF field size. A 16 arcsecond window is sufficient to capture an 8 wave defocused PSF. To be conservative, we could hope that there would be no other bright objects within 16-20 arcseconds of our target star. In an early effort to establish such bounds, Bowers et al found that any object within the WFS target field should be at least 4-5 magnitudes fainter[13]. Their work was based on a JWST precursor concept call *Nexus*. Although though work gives us great insight to the impact of unwanted objects in the WFS target field, it should be revised to better address the specific JWST architecture and its requirements.

6. CLOSING REMARKS

In this paper we examined target selection criteria and imaging requirements for JWST fine phasing. Through Monte Carlo studies we found that the impacts from systematic and stochastic effects can be managed through proper selection of the WFS target imaging parameters. In particular, we find that it is important to use sufficiently high defocus to ensure that impacts of optical bandwidth are not significant but not so much defocus as to lose sensitivity at the lowest spatial frequencies. To this end, we feel that ±6 wave defocused PSFs imagery with at most a 5% bandwidth filter can provide a WFS performance that is best matched to the JWST requirements.

Although we explored a range of aberrations magnitudes, we did not really push the limits how large aberrations are allowed to be. In other efforts, it has been found that using higher levels of defocus helped to ensure successful WFS in the presence of high-dynamic range aberrations[14,15]. The limiting dynamic range that can ultimately be sensed is

referred to as the capture range. At some point before the defocus lenses are designed, the interaction between the WFS capture range and the level of defocus diversity must be considered.

ACKNOWLEDGEMENTS

The research described in this paper was carried out at the Jet Propulsion Laboratory, California Institute of Technology, under a contract with the National Aeronautics and Space Administration.

REFERENCES

1. D. C. Redding, et al, "Next Generation Space Telescope wavefront sensing and control", Proc. SPIE, vol. 4850 (Waikoloa 2002).
2. S. A. Basinger, D. C. Redding, A. E. Lowman, L. A. Burns, K. Liu and D. Cohen, "Performance of wave front sensing and control algorithms on a segmented telescope testbed," Proc. SPIE, *UV, Optical and IR Space Telescopes and Instruments*, vol. 4013, pp. 749-756 (2000).
3. A. E. Lowman, D. C. Redding, S. A. Basinger, D. Cohen, J. A. Faust, J. J. Green, C. Ohara, F. Shi, "Phase Retrieval Camera for Testing NGST Optics," Proc. SPIE, *Astronomical Telescopes and Instruments*, Waikoloa, HI, August 22-28 (2002).
4. J. J. Green, D. C. Redding, Y. Beregovski, Andrew E. Lowman and Catherine M. Ohara, "Interferometric validation of image based wavefront sensing for NGST," Proc. SPIE, vol. 4850 (Waikoloa 2002).
5. J. J. Green, D. C. Redding, S. Shaklan and S. A. Basinger, "Extreme Wave Front Sensing Accuracy for the Eclipse Coronagraphic Space Telescope," Proc. SPIE, vol. 4860 (Waikoloa 2002).
6. J. Trauger, et al, "Eclipse high-contrast imaging test bed," Proc. SPIE, vol. 4854 (Waikoloa 2002).
7. J. J. Green, S. A. Basinger, D. Cohen, A. F. Niessner, D. C. Redding, S. B. Shaklan and J. T. Trauger, "Demonstration of extreme wavefront sensing performance on the TPF high contrast imaging testbed," Proc. SPIE, vol. 5170 (San Diego 2003).
8. J. D. Gaskill, *Linear Systems, Fourier Transforms, and Optics*, John Wiley & Sons, New York, 1978.
9. Chanan G. and Troy, M., "Strehl ratio and modulation transfer function for segmented mirror telescopes as functions of segment phase error," Applied Optics, Vol 38 num 31, pp. 6642-47, November 1999.
10. R. J. Noll, "Zernike polynomials and atmospheric turbulence," J. Opt. Soc. Am., vol. 66(3), pp. 207-211, 1976.
11. B. H. Dean & C W. Bowers, "Diversity selection for phase-diverse phase retrieval", J. Opt. Soc. Am. A., vol 20, pp. 1490-1504, August 2002.
12. A. J. Pickles, "A Stellar Spectral Flux Library, 1150 -- 25000 Å," PASP, 110, 863, 1998.
13. C. Bowers and D. Lindler, "NEXUS REPORT: Effect of Additional Field Stars on Phase Retrieval I," *Internal Memorandum*, July 2000.
14. D. Cohen and D. C. Redding, "NGST high dynamic range unwrapped phase estimation," Proc. SPIE, vol. 4850 (Waikoloa 2002).
15. C. M. Ohara, et al, "Phase retrieval camera testing of the Ball Advanced Mirror System Demonstration," Proc. SPIE, vol. 5487 (Glasgow 2004).